Section 2

Data sets, diagnostic and dynamical investigations, statistical post-processing, reanalysis, and associated studies.

FIRST AND SECOND-ORDER TRENDS OF AIR TEMPERATURE AT THE SURFACE LEVEL FROM GLOBAL RADIOSONDE DATA

O. A. Aldukhov and I. V. Chernykh
Russian Institute of Hydrometeorological Information – World Data Center, Obninsk, Russia, E-mail: aoa@meteo.ru, civ@meteo.ru

Introduction

The information about temperature trends at the surface level determined from independent datasets is important in studying global climate change and solving practical problems. The paper presents long-term trends in the time series of temperature (T) and its variability (σ) at the surface level (1-st order trends) over the Globe and the estimates of their changes depending on the trend computing period (trends of the 2-nd order).

Data and methods

The calculations are based on the radiosonde data from the CARDS aerological dataset [1] that were updated by current data from datasets AROCTAB [2] and AROCTAC [3] for the observational period of 1964–2018. The data underwent a complex quality control procedure [1]. The necessary condition for including the global aerological network station in the research was 15-year observations for the full period including 2018. The dataset from 774 stations of the global aerological network was formed after several stages of data proceeding. About 18794 thousand observations were used in this research.

The linear approximation $\tilde{T}(t,t_0,t_1)$ for the temperature $T(t)$ in the time interval $t \in [t_0,t_1]$:

$$\tilde{T}(t,t_0,t_1) = a_1(t_0,t_1)\cdot t + b_1(t_0,t_1), \quad t_0 \le t \le t_1$$

minimizes

$$\int_{t_0}^{t_1} \left(\tilde{T}(t,t_0,t_1) - T(t)\right)^2 \cdot dt \to \min .$$

The coefficient $a_1(t_0,t_1)$ is the 1-st order trend. It indicates the average rate of $T(t)$ changes in the studied time interval $[t_0,t_1]$ and corresponds to the classical linear trend. How does the rate of $T(t)$ changes depend on the initial point t_0 as it approaches the fixed end t_1 of the time interval?

The same procedure of linear approximation is applied to the 1-st order trends $a_1(\tau,t_1)$:

$$\tilde{a}_1(\tau,t_0,t_1) = a_2(t_0,t_1)\cdot \tau + b_2(t_0,t_1), \quad \tau \in [t_0,t_1].$$

The coefficient $a_2(t_0,t_1)$ is the 2-nd order trend. It indicates the average rate of the 1-st order trend changes depending on how close is the initial point t_0 to the fixed end t_1 of the time interval $[t_0,t_1]$, i.e. $a_2(t_0,t_1)$ shows the average acceleration of $T(t)$ changes with respect to the fixed end point t_1.

The trends were estimated for each of 774 stations. The monthly anomalies and their variability were calculated with respect to the long-term monthly mean values T for the full period. The values obtained for each station were annually averaged taking into account the area of the station influence.

Results

Figure 1 shows the 1-st order (a) and the 2-nd order (b) trends for the time series of the annual mean temperature anomalies and smoothed approximations of the corresponding time series. The linear trends of the 1-st and the 2-nd order for the entire period are equal to 0.12 C°·Dec^{-1} and 0.054 C°·Dec^{-2}, respectively. Figure 1 also shows the 1-st order (c) and the 2-nd

order (d) trends for the time series of mean annual monthly variability of T, they are equal to -0.053 $C^{o}\cdot Dec^{-1}$ (Figure 1c) and 0.016 $C^{o}\cdot Dec^{-2}$ (Figure 1d). All these trends are determinated with the significance of 99%.

Conclusions

The real global warming at the ground surface (Figure 1a) is detected along with the temperature variability decrease (Figure 1c); the corresponding 1-st order trends are positive and negative, respectively. According to Figure 1b (see blue line), the most significant increase in the warming rate is detected beginning in 2002. According to Figure 1d (see blue line), the 1-st order trends of temperature variability, being negative, turn to positive values beginning in about 1991. As a result, the 2-nd order trend of temperature variability (green lines) becomes slightly positive.

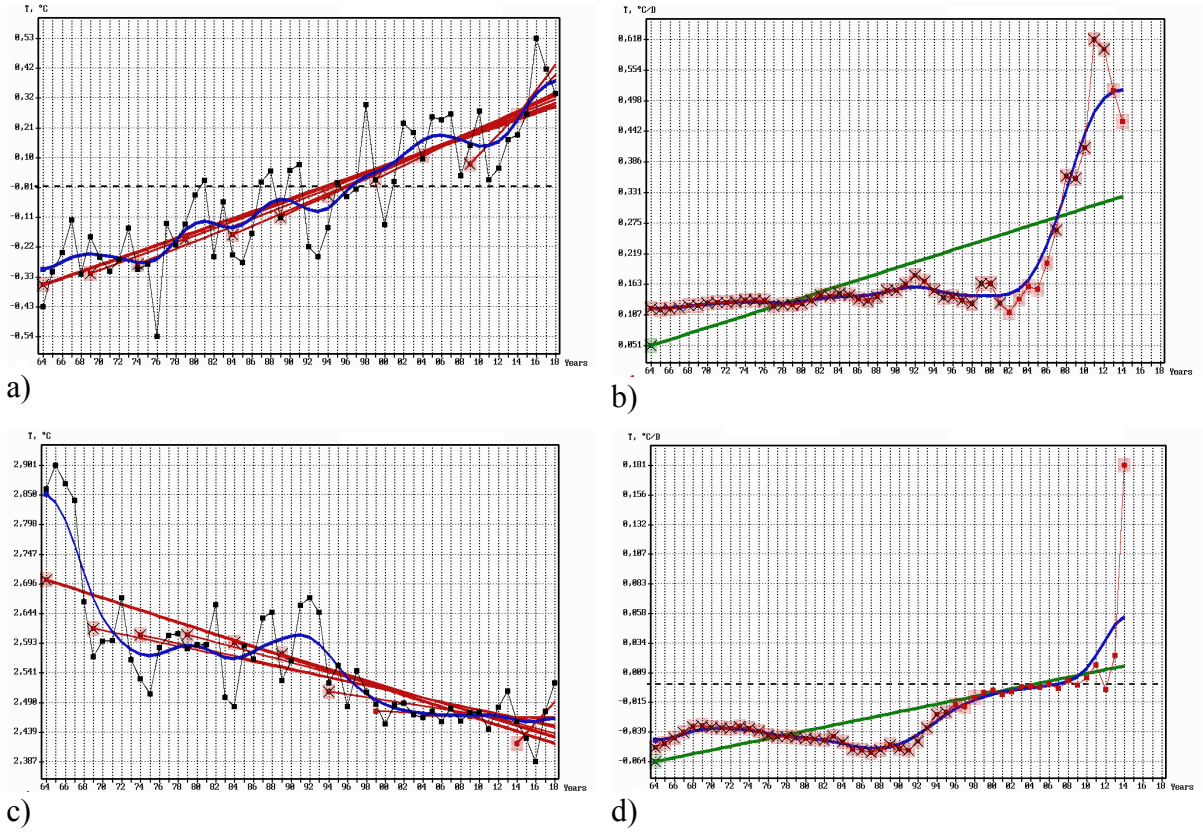

Figure 1. The 1-st and the 2-nd order trends for temperature - (a, b), for temperature variability (σ) - (c, d). Black points (a, c) are the observed annual time series, red lines (a, c) and red points (b, d) are the time series of the 1-st order trends for the corresponding periods with the 5-year step (a, c) and one-year step (b, d), blue lines are the relevant smoothed approximations of the time series, green lines (b, d) are the 2-nd order trends.

References

1. Eskridge R.E., Alduchov O.A., Chernykh I.V., Zhai P., Polansky A.C., Doty S.R. A comprehensive aerological reference dataset (CARDS): rough and systematic errors // Bull. Amer. Meteor. Soc. 1995. **76.** 1759-1775.
2. Aldukhov O.A. et al. Dataset of current aerological information AROCTAB. Description of the dataset. – Obninsk, RIHMI-WDC, 1990, 28 p.
3. Rudenkova T.V. Format for archiving of the current aerological data, received from GTS for PC // Proc. RIHMI-WDC, 2010, N 174, p. 41—63.

INFLUENCE OF ATLANTIC INFLOW ON FRESHWATER CONTENT IN THE ARCTIC OCEAN

G.V. Alekseev[1], A.V. Pnyushkov[1,2], A.V. Smirnov[1], A.E. Vyazilova[1], N.I. Glok[1]

[1] — Arctic and Antarctic Research Institute, St. Petersburg, Russian Federation (alexgv@aari.ru)

[2] — International Arctic Research Center, University of Alaska, Fairbanks, USA

Inter-decadal changes in the water layer of Atlantic origin and freshwater content (FWC) in the upper 100 m layer were traced jointly to assess the influence of inflows from the Atlantic on FWC changes based on oceanographic observations in the Arctic basin for the 1960s – 2010s decades. For this assessment, we used oceanographic data collected at the Arctic and Antarctic Research Institute (AARI) and the International Arctic Research Center (IARC).

The results demonstrated that the upper boundary of the Atlantic water (AW) layer, identified with the depth of zero isotherm, raised everywhere by several tens of meters in 1990s – 2010s, when compared to its position before the start of warming in the 1970s (Fig. 1 a-d). The lower boundary of the AW layer, also determined by the depth of zero isotherm, became deeper. Such displacements of the layer boundaries indicate an increase in the volume of the Atlantic water in the Arctic basin coming through Fram Strait and the Barents Sea. As a result, the balance of water masses was disturbed and its restoration had to occur due to the reduction of the volume of the upper most dynamic freshened layer [1-3]. Accordingly, the content of fresh water in this layer should decrease, if it does not make up by the growth of fresh water from rivers and precipitation. We show that FWC has decreased in the 50–100 m layer in the Eurasian part of the Arctic Basin to the west of 180°E in the 1990s (Fig. 1 e-h). In contrast, the FWC to the east of 180°E and closer to the shores of Alaska and the Canadian archipelago increased. These opposite tendencies have been intensified in the 2000s and the 2010s. The influence of fresh water influx manifested clear as an increase in water storage in the Canadian Basin and the Beaufort Gyre in the 2000s – 2010s (Fig.1 g, h).

Conclusions

The warming detected in the early 1990s in the layer of water of Atlantic origin north of the Kara Sea was traced throughout the Arctic basin in all subsequent decades including the 2010s. Large-scale changes in the AW layer affected the vertical structure of the entire water column in the Arctic Ocean. The upper boundary of the AW layer lifted up everywhere for several tens of meters compared to its position in the 1970s before the start of the AW warming. At the same time, the lower boundary of the AW layer became deeper as a result of the enhanced transport of the transformed AW through the Barents and Kara Seas. The FWC in the 50–100 m

layer decreased in the Eurasian part of the Arctic basin to the west of 180° E. Contrary, in the Canadian basin the FWC increased. The influence of freshwater influx on FWC changes was manifested as an increase in the water content in the Canadian Basin and the Beaufort Gyre in the 1990s - 2010s, which may be partly a consequence of the increase of the AW inflow into the North European basin, alongside an increase in cyclonicity over the Arctic basin and heat and moisture transports through the Atlantic sector of the Arctic Ocean.

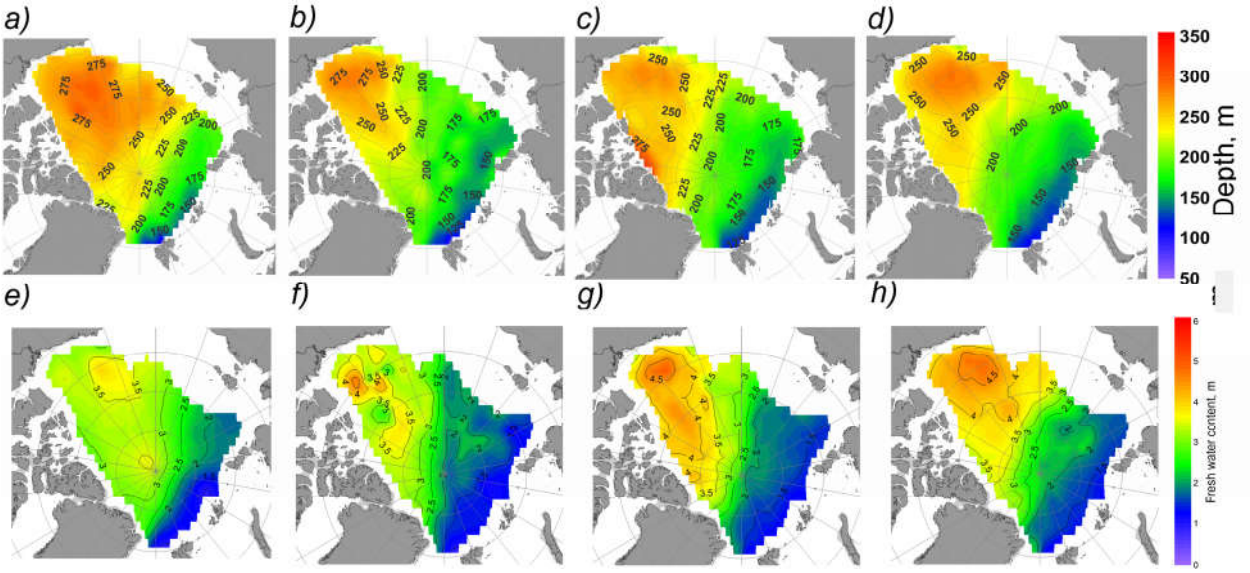

Fig. 1. The depth of the upper boundary of the AW layer in decades: a — the 1970s, b — the 1990s, c — the 2000s, d — the 2010s. The fresh water content in the 50–100 m layer in decades: e — the 1970s, f — the 1990s, g — the 2000s, h — the 2010s

Acknowledgments. The research is supported by the Russian Foundation for Basic Research, Project 18-05-60107.

References

Häkkinen S., Proshutinsky A. Freshwater content variability in the Arctic Ocean // J. Geophys. Res. Ocean. 2004. V. 109. C3.

Muilwijk M., Smedsrud L.H., Ilicak M., Drange H. Atlantic Water Heat Transport Variability in the 20th Century Arctic Ocean From a Global Ocean Model and Observations // J. Geophys. Res. Ocean. 2018. V. 123, № 11. P. 8159–8179.

Alekseev G.V., Pnyushkov A.V., Smirnov A.V., Vyazilova A.E., Glok N.I. Influence of Atlantic inflow on the freshwater content in the upper layer of the Arctic basin. Problemy Arktiki i Antarktiki. Arctic and Antarctic Research. 2019, 65 (4): 363–388. [In Russian]. doi: 10.30758/0555-2648-2019-65-4-363-388

SPATIOTEMPORAL DISTRIBUTIONS OF GLOBAL TRENDS OF HUMIDITY AND TEMPERATURE IN THE LOW TROPOSPHERE

I. V. Chernykh and O. A. Aldukhov
Russian Institute of Hydrometeorological Information – World Data Center, Obninsk, Russia, E-mail: civ@meteo.ru, aoa@meteo.ru,

Introduction

The estimations of long-term changes in humidity and temperature (T) distributions in the low troposphere obtained on the basis of hourly values are necessary for investigations of global climate change. The paper presents the series of the 1-st and 2-nd order trends [1] of temperature, absolute (AH) and relative (RH) humidity in the global layer 0-2 km above the surface for different months and seasons in the Northern hemisphere for the period of 1964–2018.

Data and methods

Reported observations from the CARDS global aerological dataset [2] that were updated by current data from RIHMI-WDC for the period of 1964–2018 were used in this research. The computations are based on the radiosonde dataset from 774 appropriate stations with relatively homogeneous observations. The necessary condition for including a station in the research was 15-year observations from the full period including 2018.

The Akima cubic spline interpolation method was used to calculate AH, RH, T values and their variations (σ) in the layer 0–2 km over the surface taking into account standard levels and specific points of vertical profiles. The trends were estimated for each station by using the least squares method. The anomalies were calculated with respect to the corresponding long-term mean values for the period of 1964–2018. The values obtained for all stations were averaged taking into account the area of the station influence.

Results

Figure 1 shows that the spatiotemporal distributions of the 1-st order trends (classical linear trends) for anomalies and variations of the studied parameters are nonuniform in the layer 0–2 km above the surface. The annual changes of the 1-st order trends of the long-term monthly means anomalies in the 0–2-km layer range from -1.54 to 5.68 $100 \cdot g/m^3$ per decade for AH, from -0.69 to 0.11 %/decade for RH, and from 0.08 to 0.16 C°/decade for T. The global absolute humidity in this layer increases mainly at 0.4–1.1 km for all months, at 1.1–1.7 km in summer, and near the surface in summer and autumn. The temperature increases mainly at 1.5–2 km above the surface for all months and at 0–0.1 km in winter and autumn. The relative humidity increases only at 0.5–0.9 km, the largest decrease of RH is detected from October to April at 1.6–2 km.

The 1-st order trends of variability (σ) of all studied parameters are negative for all months in the entire 0–2 km layer. The most intense decrease of variability is detected for AH at 0.0–1.2 km in summer, for RH near the surface (0-50 m) and at 0.8–1.4 km, and for T throughout the layer 0–2 km in winter and at 0.6–2 km in spring and autumn.

Time series of the 1-st order trends for the different starting year and the 2-nd order trends for AH (a), RH (b), T (c) for the whole period of 1964-2018 at the 0.6 km level are presented in Figure 2. The 2-nd order trends for all parameters are positive, which means the acceleration of changes for all values with the year 2018 approaching. Figure 2 also shows critical changes of the 1-st order trends in 2002 for all parameters and in 1980 and 2008 for humidity.

Conclusions

The spatiotemporal distributions of the linear trends of absolute and relative humidity and temperature anomalies are not uniform in the tropospheric layer 0–2 km over the Globe. The absolute and relative humidity increases mainly at the heights of 0.4–1.1 km for all months,

and temperature grows near the surface in winter and autumn and at 1.5–2 km above the surface for all months.

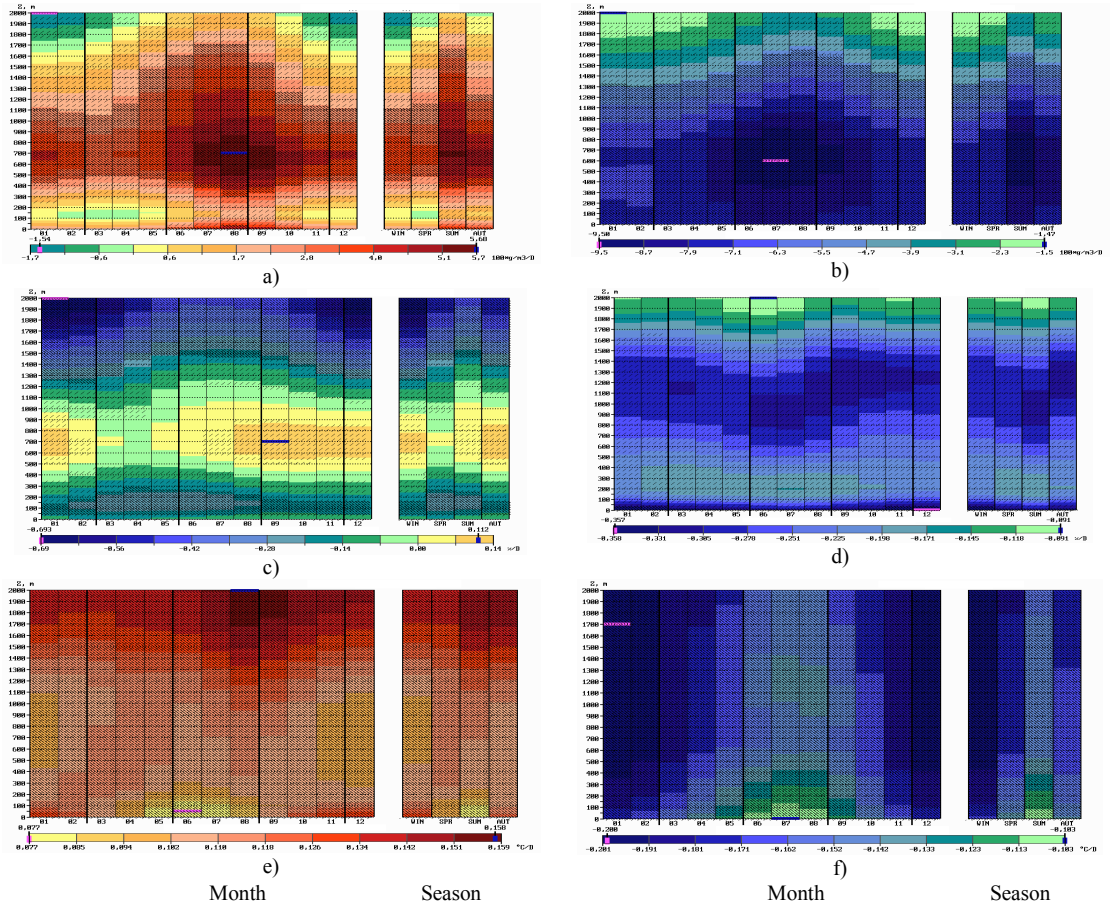

Figure 1. First-order trends of anomalies of long-term means (a, c, e) for AH (a, 100·g/m^3 /decade), RH (b, %/decade), T (e, Cº/decade) and first-order trends of variability (b, d, f) for AH, RH, T in the low tropospheric layer 0–2 km for every month and season. The global statistics for months and seasons were subject to twofold smoothing. The three–points smoothing was used. Trends with significance of not less than 50% are marked by the sloping line segments and with significance of not less than 95% – by lattice. Blue and pink segments correspond to maximum and minimum values. 1964–2018.

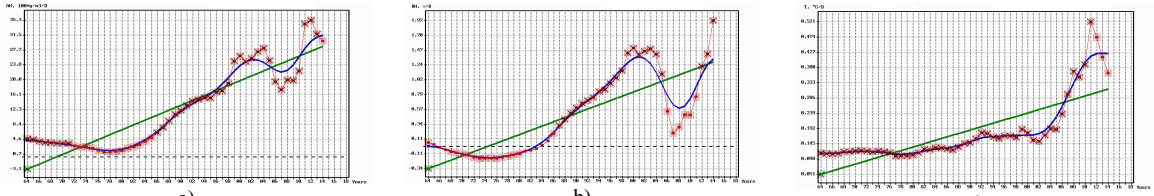

Figure 2. First and 2-nd order annual trends for AH (a), RH (b), T (c) at 0.6 km. Red lines and red points are the time series of the 1-st order trends for the corresponding periods with the one-year step, blue lines are the corresponding smoothed approximation of time series, green lines are the 2-nd order trends.

References

1. Aldukhov O.A., Chernykh I.V. First and second-order trends of air temperature at the surface level from global radiosonde data // This volume, pp. 2-03-2-04.
2. Eskridge R.E., et. al. A comprehensive aerological reference dataset (CARDS): rough and systematic errors // Bull. Amer. Meteor. Soc. 1995. **76.** 1759-1775.

The associations of winter Atlantic SST, Arctic sea ice, and East Asian surface temperature

Muyuan Li [1, 2, 3], Dehai Luo [2, 3], Ian Simmonds [1], Aiguo Dai [4],
Linhao Zhong [2] and Yao Yao [2]

[1] School of Earth Sciences, The University of Melbourne, Victoria, Australia
simmonds@unimelb.edu.au
[2] CAS Key Laboratory of Regional Climate-Environment for Temperate East Asia, Institute of Atmospheric Physics, Chinese Academy of Sciences, Beijing, China
[3] University of Chinese Academy of Sciences, Beijing, China
[4] Department of Atmospheric and Environmental Sciences, University at Albany, SUNY, Albany, NY, USA

We are investigating the physical processes underlying recent winter cold anomalies over East Asia (EA). The Arctic region has experienced a rapid loss of sea ice in winter since the 1990s (Simmonds 2015), whereas EA has shown a large cooling trend during the winter months (Yao et al. 2017; Luo et al. 2017). Considerable research has been devoted to determining if there is a direct connection between these two occurrences, and what mediating factors might be present (Screen and Simmonds 2013; Luo et al. 2019a, b), such as high-latitude blocking (Luo et al. 2017, 2018). In addition, there is some evidence to indicate that anomalies in the North Atlantic Ocean can initiate teleconnection wave trains that can influence both Arctic sea ice and Eurasian climate (Simmonds and Govekar 2014; Luo et al. 2016, 2017).

Our analysis is aimed at determining which specific aspects of Atlantic SST variability might be linked to Arctic ice loss. We have undertaken this by decomposing winter SST variability into its first four EOF modes (Fig. 1) and exploring the 'downstream' impacts of each of these separately. Each mode induces a different large-scale circulation response. It is shown that the extent to which temperature over EA is impacted, in turn strongly depends on whether the sea ice anomalies are able to set up a persistent anticyclonic structure (or 'block') over the Ural Mountains region of western Russia (at about 60°E). Full details of the investigation are presented in Li et al. (2020).

References

Li, M. et al., 2020: Anchoring of atmospheric teleconnection patterns by Arctic sea ice loss and its link to winter cold anomalies in East Asia. *Int. J. Climatol.*, doi: 10.1002/joc.6637.

Luo, B. et al., 2017: Atmospheric circulation patterns which promote winter Arctic sea ice decline. *Env. Res. Lett.*, **12**, 054017, doi: 10.1088/1748-9326/aa69d0.

Luo, B. et al., 2019: The winter midlatitude-Arctic interaction: Effects of North Atlantic SST and high-latitude blocking on Arctic sea ice and Eurasian cooling. *Climate Dyn.*, **52**, 2981-3004, doi: 10.1007/s00382-018-4301-5.

Luo, D. et al., 2018: Changes in atmospheric blocking circulations linked with winter Arctic warming: A new perspective. *J. Climate*, **31**, 7661-7678.
Luo, D. et al., 2017: Increased quasi-stationarity and persistence of winter Ural Blocking and Eurasian extreme cold events in response to Arctic warming. Part II: A theoretical explanation. *J. Climate*, **30**, 3569–3587, doi: 10.1175/JCLI-D-16-0262.1.
Luo, D. et al., 2016: Impact of Ural Blocking on winter Warm Arctic–Cold Eurasian anomalies. Part II: The link to the North Atlantic Oscillation. *J. Climate*, **29**, 3949-3971.
Luo, D. et al., 2017: Winter Eurasian cooling linked with the Atlantic Multidecadal Oscillation. *Env. Res. Lett.*, **12**, 125002, doi: 10.1088/1748-9326/aa8de8.
Luo, D. et al., 2019: Weakened potential vorticity barrier linked to recent winter Arctic sea ice loss and midlatitude cold extremes. *J. Climate*, **32**, 4235-4261.
Screen, J. A., and I. Simmonds, 2013: Caution needed when linking weather extremes to amplified planetary waves. *Proc. Nat. Acad. Sci. USA*, **110**, E2327.
Simmonds, I., 2015: Comparing and contrasting the behaviour of Arctic and Antarctic sea ice over the 35-year period 1979-2013. *Ann. Glaciol.*, **56(69)**, 18-28.
Simmonds, I., and P. D. Govekar, 2014: What are the physical links between Arctic sea ice loss and Eurasian winter climate? *Env. Res. Lett.*, **9**, 101003.
Yao, Y. et al., 2017: Increased quasi-stationarity and persistence of winter Ural Blocking and Eurasian extreme cold events in response to Arctic warming. Part I: Insights from observational analyses. *J. Climate*, **30**, 3549–3568, doi: 10.1175/JCLI-D-16-0261.1.

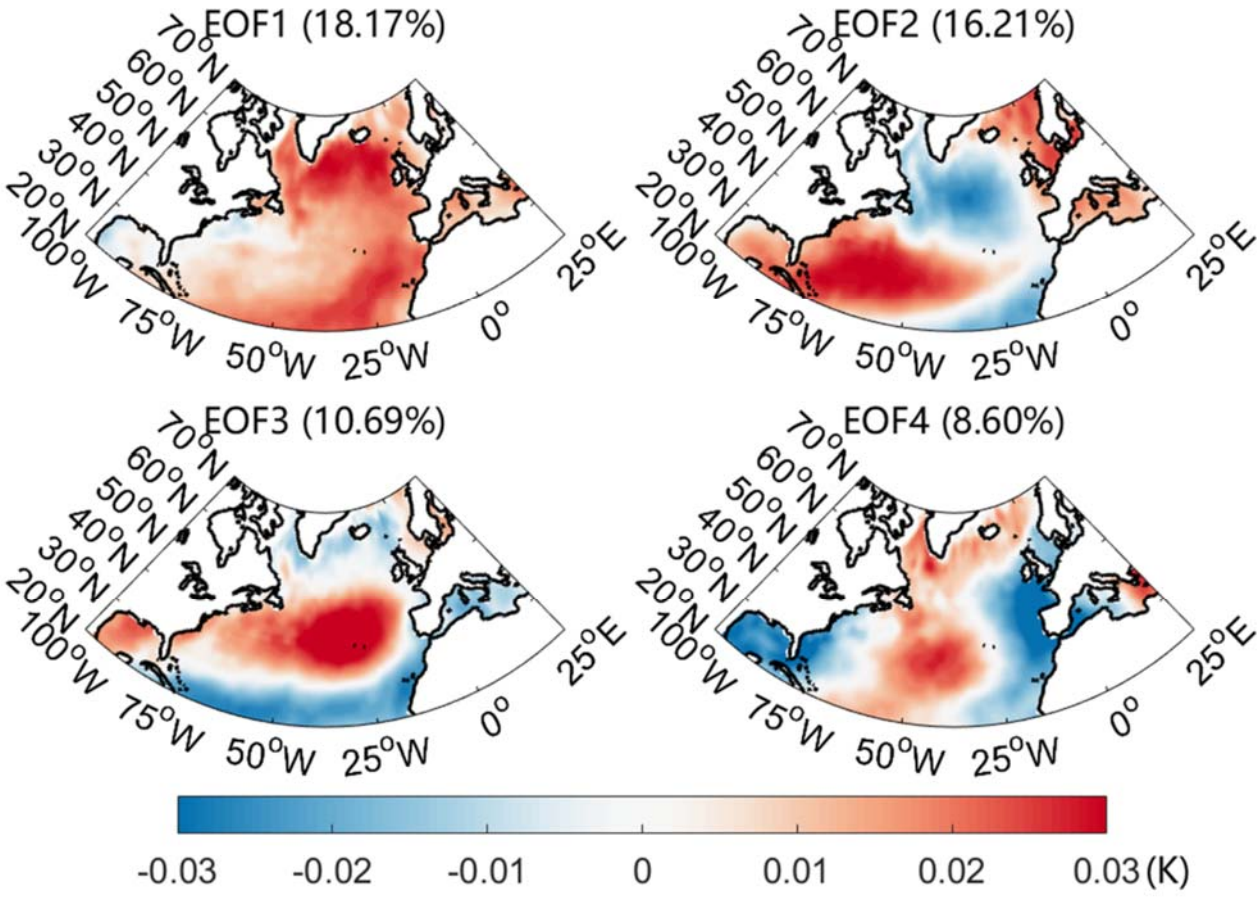

Fig. 1: First four EOFs of detrended and normalized winter (DJF) SST anomalies (for the period 1958–2016).

Estimates of the contribution of key natural modes and anthropogenic forcing to global surface temperature trend at different temporal horizons

I.I. Mokhov[1,2] and D.A. Smirnov[3]
[1]A.M. Obukhov Institute of Atmospheric Physics RAS, Moscow, mokhov@ifaran.ru
[2]Lomonosov Moscow State University, Moscow
[3]Saratov Branch of V.A. Kotel'nikov Institute of RadioEngineering and Electronics RAS, Saratov, smirnovda@yandex.ru

The contribution of changes in radiative forcing (RF) associated with changes in the concentration of greenhouse gases (GHG) and the key natural intra-centennial modes of global and regional climate variability to the global surface air temperature (GST) trend at different time horizons is estimated. Estimates are performed from the average annual data for the GST for the period 1850-2017 (http://www.metoffice.gov.uk/hadobs/hadcrut4/). Anthropogenic influence is characterized by the GHG RF for the period 1851-2012 (http://data.giss.nasa.gov/). The key modes of natural climatic variability are characterized by the Atlantic Multidecadal Oscillation (AMO) index for the period 1856-2017, Pacific Decadal Oscillation (PDO) index for the period 1854-2017 and El Nino/Southern Oscillation (ENSO) index Nino-3.4 for the period 1870-2017 (http://www.esrl.noaa.gov/psd/data/). The contributions are estimated as the changes of the model trends under different conditions over various time windows (temporal horizons).

The intervals used for the GST trends estimation range from several years to several decades. The empirical models of the GST used for the estimation are three-component autoregressive (AR) models with the account of the influence of the GHG RF, AMO, PDO and ENSO effects similarly to Refs. [1,2]. The optimal empirical model relating the GST to AMO and GHG RF (for maximum lags up to 25 years) takes the following form:

$$T_n = a_0 + a_1 T_{n-1} + a_2 I_{GHG,n-16} + a_3 I_{AMO,n-23} + \xi_n, \quad (1)$$

where T is the GST, n is the discrete time (years), I_{GHG} is the GHG RF, I_{AMO} is the slow AMO component, ξ_n is noise (residual model errors). When estimating with a maximum lag of 23 years from the whole period under analysis, the values of the coefficients in (1) with their 95% confidence intervals appear as follows: a_0 = -0.22 (±0.07) K, a_1 = 0.41 (±0.16), a_2 = 0.18 (±0.05)K/(Wm^{-2}), a_2 = -0.21 (±0.15), the mean squared prediction error (MSE) equals 0.0096 K^2.

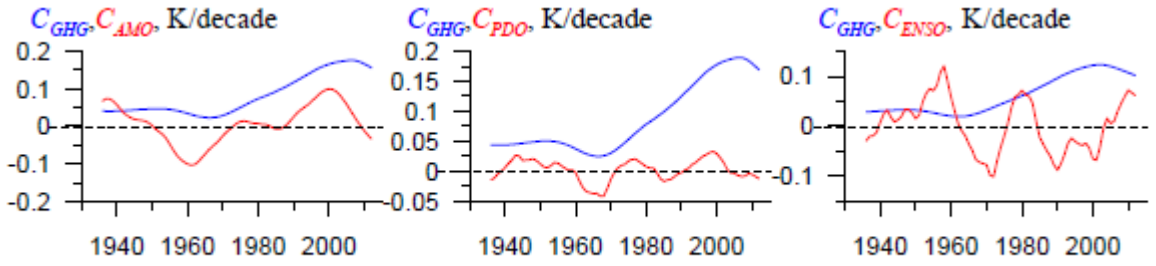

Figure 1. (a) (b) (c)

Figure 1a shows the estimated contribution of AMO (red) and GHG RF (blue) to the GST trend over 15-year time windows versus the window endpoint. The estimates are computed as the difference between the model GST responses to the actually observed forcings and the hypothetical forcings, the latter being the constant GHG RF at the level of 1850 and constant AMO index at its mean observed value.

Analogous results for the other models analyzed here are reported below in a similar form. Thus, the AR model corresponding to (1) but with unit time lags reads

$$T_n = a_0 + a_1 T_{n-1} + a_2 I_{GHG,n-1} + a_3 I_{AMO,n-1} + \xi_n, \quad (1a)$$

with a_0 = -0.22 (±0.08) *K*, a_1 = 0.43 (±0.18), a_2 = 0.14 (±0.05) *K*/(Wm^{-2}), a_3 = 0.22 (±0.16), and the MSE of 0.0101 K^2. It gives slightly less accurate forecast than model (1).

The optimal AR model for the GST with the PDO index I_{PDO} and GHG RF reads

$$T_n = a_0 + a_1 T_{n-1} + a_2 I_{GHG,n-16} + a_3 I_{PDO,n-12} + \xi_n, (2)$$

with a_0 = -0.20 (±0.07) *K*, a_1 = 0.48 (±0.16), a_2 = 0.17 (±0.05) *K*/(Wm^{-2}), a_3 = 0.01 (±0.02), and the MSE of 0.0108 K^2. Figure 1b shows estimates of contribution of PDO (red) and GHG RF (blue) to the GST trend in 15-year windows with the use of model (2). The corresponding model with unit lags reads

$$T_n = a_0 + a_1 T_{n-1} + a_2 I_{GHG,n-1} + a_3 I_{PDO,n-1} + \xi_n, \quad (2a)$$

with a_0 = -0.17 (±0.07) *K*, a_1 = 0.58 (±0.15), a_2 = 0.11 (±0.04) *K*/(Wm^{-2}), a_3 = -0.00 (±0.02), and the MSE of 0.0107K^2.

The optimal AR model for the GST with the ENSO index I_{ENSO} and GHG RF reads

$$T_n = a_0 + a_1 T_{n-1} + a_2 I_{ENSO,n-2} + a_3 I_{GHG,n-10} + \xi_n, (3)$$

with a_0 = -0.08 (±0.06) *K*, a_1 = 0.77 (±0.13), a_2 = -0.07 (±0.03), a_3 = 0.05 (±0.04)*K*/(Wm^{-2}) and the MSE of 0.0111K^2. Figure 1c shows the estimated contribution of ENSO (red) and GHG RF (blue) to the GST trend in 15-year windows with the use of model (3). The corresponding model with unit time lags reads

$$T_n = a_0 + a_1 T_{n-1} + a_2 I_{GHG,n-1} + a_3 I_{ENSO,n-1} + \xi_n, \quad (3a)$$

with a_0 = -0.11 (±0.06) *K*, a_1 = 0.67 (±0.14), a_2 = 0.07 (±0.04) *K*/(Wm^{-2}), a_3 = 0.02 (±0.04) and the MSE of 0.0124 K^2.

According to the obtained estimates the optimal time lag in AR models is 23 years for the AMO, 12 years for the PDO, 2 years for the ENSO, ranging from 10 to 16 years for the GHG. For 15-year intervals, the contribution of the AMO reaches the value of 0.1 K/decade, the contribution of the PDO is insignificant (less than 0.03 K/decade), and the GHG contribution reaches 0.2 K/decade. The GHG contribution over 15-year intervals is comparable to the contribution of the AMO and the ENSO with the contribution of the PDO being insignificant. With widening the temporal interval over which the contribution to the GST trend is estimated, the contribution of the AMO and the ENSO decreases, the GHG contribution dominating over long temporal intervals.

The signal processing and interpretations were carried out within the framework of the RFBR projects (17-29-05098, 18-05-60111). The analysis of causal relationships was carried out as a part of the Russian Science Foundation project (grant 19-17-00240).

References

1. Mokhov I.I., Smirnov D.A. (2018) Estimating the contributions of the Atlantic Multidecadal Oscillation and variations in the atmospheric concentration of greenhouse gases to surface air temperature trends from observations. *Doklady Earth Sci.*, **480** (1), 602–606.
2. Mokhov I.I., Smirnov D.A. (2018) Contribution of greenhouse gas radiative forcing and Atlantic Multidecadal Oscillation to surface air temperature trends. *Russ. Meteorol. Hydrol.*, **43** (9), 557–564.

Strong squalls in Moscow region in 2017 and 2018

Mokhov I.I.[1,2], Timazhev A.V.[2], Yushkov V.P.[1], Babanov B.A.[1]

[1]Lomonosov Moscow State University
[2]A.M. Obukhov Institute of Atmospheric Physics RAS
mokhov@ifaran.ru

The results of the analysis of a strong squall with a hurricane wind speed (more than 32 m/s) at 15.39 on May 29, 2017 were presented in [1]. This analysis was based on regular measurements of wind speed using an ultrasonic anemometer (50 Hz) at the Physics Faculty of the Lomonosov Moscow State University (PF MSU) on the Vorob'evy (Leninskie) Gory (55°42'00.28" N, 37°31'45.30" E) at an altitude of 50 m above the surface. Similar measurements were carried out on April 21, 2018, when a hurricane wind speed was also recorded at the time of the strongest squall at 17.04 PM. Here we present the results of the corresponding analysis of sudden changes in wind speed associated with the strong squall in Moscow in April 2018. The predictability of such strong squalls with great destructive power, which are among the most dangerous meteorological phenomena in mid-latitudinal regions, is of particular importance.

Figure 1 shows the variations of the zonal (U) and meridional (V) wind components, as well as the vertical velocity (W) for three hours (15.30-18.30 PM) on 21 April, 2018 by measurements (without filtering) at the PF MSU. The strongest fluctuations were noted during the squall at 17.04 PM for the V-component up to hurricane velocity values (up to 32 m/s and even more). Wavelet analysis reveals cyclic changes in the components of the wind during the analyzed 3-hour time interval - with periods of about 50-60 minutes and with shorter periods.

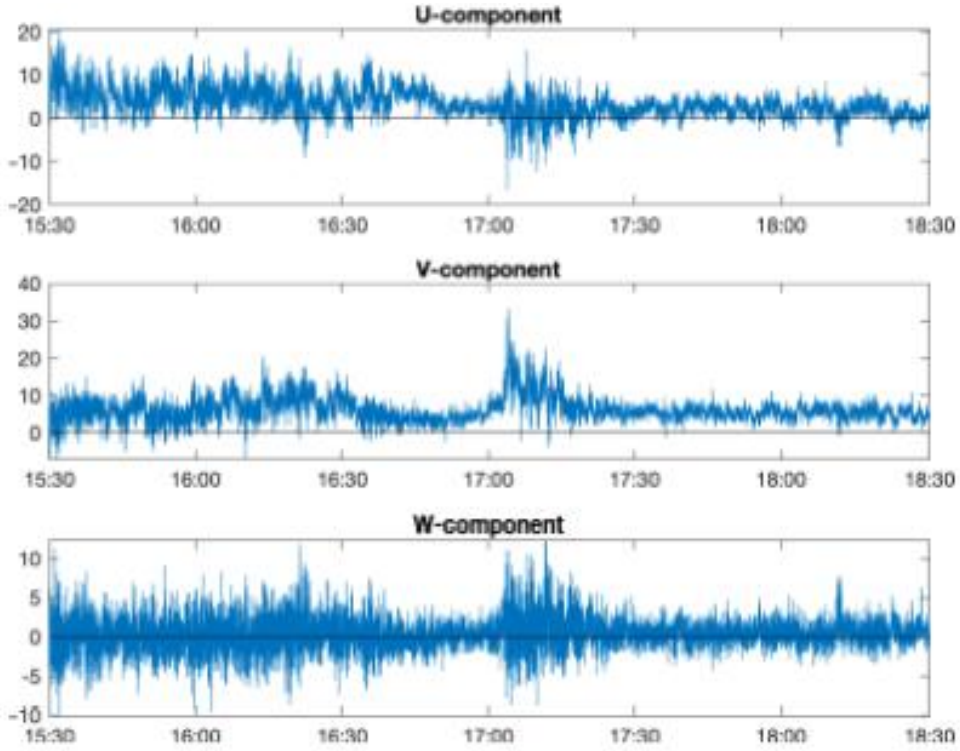

Fig. 1. Variations of the zonal (U) and meridional (V) components of the wind (m/s), as well as the vertical velocity (W) for three hours (15.30-18.30 PM) on 21.04.2018 by measurements at the PF MSU.

Cross-wavelet analysis of the mutual variations of various wind components revealed significant changes during the analyzed 3-hour time interval. Figure 2 shows the local coherence of the U- and V-components for three hours (15.30-18.30 PM) on 21 April, 2018 as measured at the PF MSU. A comparison of two strong squalls in Moscow in 2017 and 2018 revealed some differences. Figure 2 reveals a significant coherence of the U and V variations (with a negative correlation) with periods of about an hour, in contrast to the previous strong squall in Moscow. According to [1], the squall on May 29, 2017 initiated a chain of coherent variations in the U and V components of the wind speed with a positive correlation and with an increase in the characteristic period. This trend was also manifested in association with the squall in 2018, but it is less pronounced.

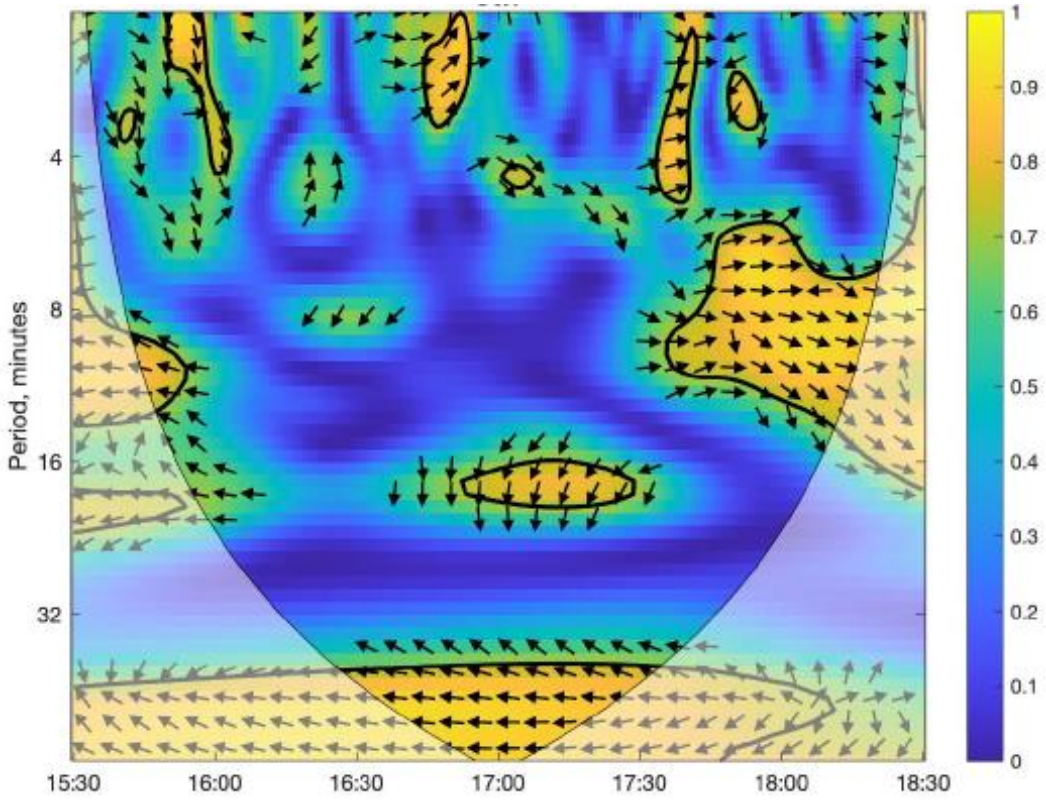

Fig. 2. Local coherence of U- and V-components for three hours (15.30-18.30 PM) on 21.04.2018 by measurements at PF MSU.

The extreme wind in Moscow in April 2018, as in May 2017, was associated with the atmospheric front. The strongest squalls noted in the spring of 2018 and 2017 are very unusual and rare in the Moscow region. The recurrence of such strong squalls within one year may be an indicator of regional weather and climate changes, especially in the spring. Also, the results indicate some predictive opportunities in assessing the risk of extreme squalls.

This analysis was performed in the framework of the RSF project 19-17-00240.

References

1. Mokhov I.I., Timazhev A.V., Yushkov V.P. (2018) Squalls with a hurricane wind in Moscow. Research Activities in Atmospheric and Oceanic Modelling. E. Astakhova (ed.). WCRP Rep. No. 15/2018. S. 2. P. 21-22.

TROPICAL CYCLONES IN THE WESTERN NORTH PACIFIC OCEAN: CHANGES OF THEIR TOTAL ACTION DURING PAST DECADES

I.I. Mokhov[1,2], A.G. Poroshenko[2]
[1]A.M. Obukhov Institute of Atmospheric Physics RAS, Moscow, Russia
[2]Lomonosov Moscow State University, Moscow, Russia
mokhov@ifaran.ru

The analysis has been performed for the tropical cyclones (TC) action S as an integral characteristic of their energy impact. Similar analysis was done in [4] for total action of atmospheric blockings and in [5] for total action of extratropical cyclones. This value S has a dimension [energy]x[time]. Action S of individual climate structure, in particular for TC, can be defined as follows

$$S \sim \int_0^\tau E(t)dt,$$

where integration over time t is performed from 0 to τ, τ is the vortex life time, E is the vortex energy. The kinetic energy of an atmospheric vortex can be expressed via $(\Delta P)^2$, where ΔP is a pressure difference between the vortex centre and periphery [1,2]. The integral action S_Σ for an ensemble of TCs is defined as a sum of values of action for individual TCs.

Here we present results of the TC action analysis for the Western North Pacific Ocean (WNPO) basin. This basin is characterized by the largest TC number N_{tc} per year. According to observations for recent decades, on average 44% of TCs in the Northern Hemisphere are formed in the WNPO [3,6]. At the same time, annually about 9 of 25 TCs in the WNPO basin are transformed into extratropical cyclones (ETC) and a significant positive trend was noted - with an increase in the number of transformation events (N_{etc}) by 1 cyclone in 14–15 years or more than 4% per decade for N_{etc}/N_{tc}. In this regard, estimates of the TCs energy are relevant, including the energy of TCs reaching extratropical latitudes, in particular in the WNPO.

Our analysis is based on the RSMC data (http://www.jma.go.jp/jma/jma-eng/jma-center/rsmc-hp-pub-eg/RSMC_HP.htm) for TCs in the WNPO for the period 1951-2019. Figure 1 shows interannual changes in the normalized TCs total action S_Σ in the WNPO during 1951-2019 with a significant increase during past three decades of the interannual variations range. According to Fig. 1, in the past three decades several times it reached and even exceeded the double mean level for the base period 1951-1980. The mean S_Σ values since the second part of 1980s are remarkably larger than for the base period despite the presence of years with very low S_Σ values.

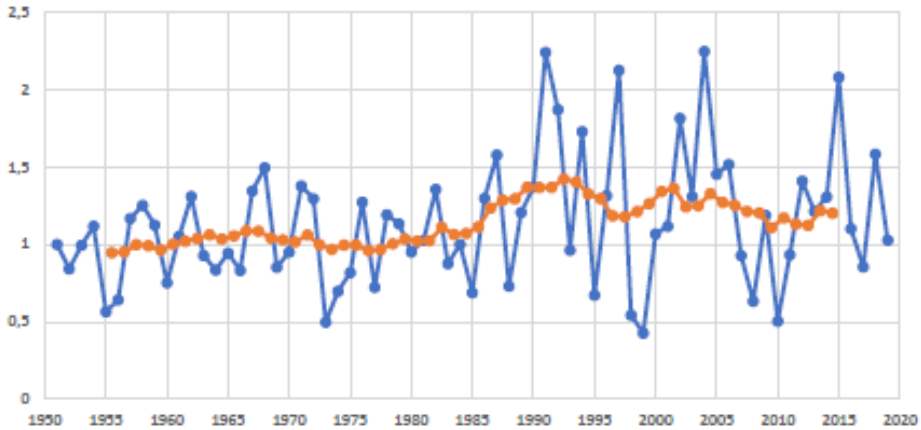

Fig. 1. Interannual changes of the normalized total action $S_\Sigma(N_{tc})$ of N_{tc} TCs in the WNPO in 1951-2019. Estimates of $S_\Sigma(N_{etc})/N_{etc}$ are normalized to the average value for the period 1951-1980 (blue line). The red line corresponds to 10-year means with moving averaging.

Figure 2 shows the interannual changes in the normalized total action $S_\Sigma(N_{etc})/N_{etc}$, corresponding to the mean individual ETC in the WNPO in 1951-2019. A general increase in $S_\Sigma(N_{etc})/N_{etc}$ during the last decades is accompanied by significant interannual variations.

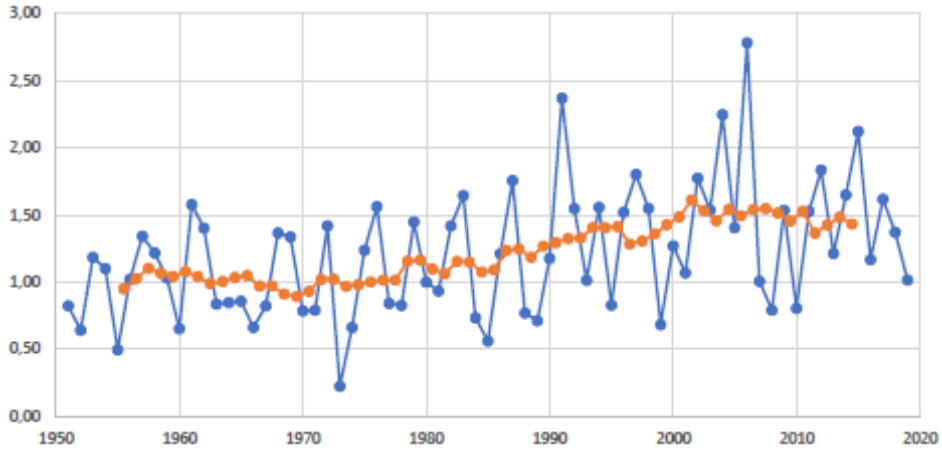

Fig. 2. Interannual changes of the normalized action $S_\Sigma(N_{etc})/N_{etc}$, corresponding to the mean individual ETC in the WNPO in 1951-2019. Estimates of $S_\Sigma(N_{etc})/N_{etc}$ are normalized to the average value for the period 1951-1980.

The results obtained for tropical WNPO cyclones indicate a high variability of their action with a general growth in recent decades and an increase in the risk of their effects in extratropical latitudes.

The analysis of tropical cyclones was carried out as part of the RSF project (19-17-00240). The analysis of extratropical cyclones transformed from tropical cyclones was carried out as a part of the RFBR project (17–29–05098).

References

1. Akperov M.G., Bardin M.Yu., Volodin E.M., Golitsyn G.S., Mokhov I.I. (2007) Probability distributions for cyclones and anticyclones from the NCEP/NCAR reanalysis data and the INM RAS climate model. *Izvestiya, Atmospheric and Oceanic Physics*, **43**, 705–712.
2. Golitsyn G.S., Mokhov I.I., Akperov M.G., Bardin M.Yu. (2007) Distribution functions of probabilities of cyclones and anticyclones from 1952 to 2000: An instrument for the determination of global climate variations. *Doklady Earth Sciences*, **413**, 324–326.
3. Intense Atmospheric Vortices and their Dynamics. Ed. by I.I. Mokhov, M.V. Kurgansky, O.G. Chkhetiani. Moscow, GEOS, 2018, 482 p. (in Russian)
4. Mokhov I.I. (2006) Action as an integral characteristic of climatic structures: Estimates for atmospheric blockings. *Doklady Earth Sciences*, **409A** (6), 925–928.
5. Mokhov I.I., Akperov M.G., Dufresne J.-L., Le Treut H. (2009) Cyclonic activity and its total action over extratropical latitudes in Northern Hemisphere from model simulations. *Research Activities in Atmospheric and Oceanic Modelling.* J. Cote (ed.). Geneva: WCRP. Rep. 39. S. 7. P.9-10.
6. Mokhov I.I., Dobryshman E.M., Makarova M.E. (2014) Extratropical transition of tropical cyclones: Tendencies of change. *Doklady Earth Sci.*, **454** (1), 59-63.

Effect from polynyas in the Siberian Arctic seas to atmospheric transport of heat and moisture

Uliana Prokhorova [1,2], Alexandra Urazgildeeva [1]

1. AARI and 2. NIERSC

E-mail: uliana@niersc.spb.ru

The decisive contribution of atmospheric meridional heat transfer (MHT) to the Arctic energy budget to the North of 70° N in winter was established in [3]. It was shown [1,2] that the main MHT in the Arctic in winter enters through the Atlantic sector at 70° N between 0° and 80° E ("Atlantic Gate") in the layer from the surface to 750 hPa. But the question remained of the lack of connection between the fluctuations in the integral transfer of sensible heat through the entire circle of 70° N and an average temperature in the region of 70- 90° N. A possible explanation for this is that the cold air transport from Eurasia through 80-150°E, where in winter south winds prevail, contributes essentially to the calculations of the total influx of sensible heat. But this influx does not have a noticeable effect on the average air temperature at 70-90 ° N due to the influx of heat from a polynya in the Arctic seas. [4]

To detect and take into account the temporal variability of the polynya position in the Laptev Sea, the HadleySST daily archive of sea ice concentration data was taken from the Met Office Hadley Center website for the period from 1979 to 2018. Based on the minimum concentrations, it was determined that the polynya considered in this study is between 110-130°E and 73-74° N. To assess the spatial variability of heat and moisture transfers we used the daily data (00 and 12 UTC) from the ERA - Interim reanalysis with a spatial resolution of 0.125x0.125°. The calculation of the meridional heat transport and moisture through 70° N and 74° N was carried out according to the method described in [1-3].

The effect of the polynya on the atmosphere is shown in spatial (latitudinal and longitudinal) profiles of temperature, humidity, and heat balance components . From Table 1, there is a noticeable change in the properties of the air mass when moving northward to 74° N is obvious: in the region of 115-130° E, the air temperature increases, as well as the outgoing longwave flux.

Table 1. Near-surface air temperature (T2M), sensible heat flux (SSHF), outgoing longwave radiation (LWU), meridional heat (TV) and moisture (QV) transport along latitudinal sections at 70 °N (land) and 74 °N (polynya) averaged over 1979 to 2018 in the Laptev sea.

	T2M		SSHF		LWU		QV		TV	
Longitude ° E	land deg.C	polynya deg. C	land W/m^2	polynya W/m^2	land W/m^2	polynya W/m^2	land kg/m/s	polynya kg/m/s	land W/m	polynya W/m
100-110	-32.6	-30.2	-14.8	-11.5	181.7	193.7	0.9	0.4	3.0	1.1
110-120	**-33.2**	**-27.1**	**-22.1**	**14.4**	**183.4**	**212.9**	**0.5**	**1.6**	**1.9**	**4.1**
120-130	**-34.3**	**-26.1**	**-19.0**	**4.7**	**177.0**	**212.6**	**1.0**	**2.3**	**4.3**	**5.8**
130-140	-35.0	-25.6	-12.4	-0.5	175.6	213.2	1.1	1.8	5.9	4.5

In the spatial distribution, the effect of the polynya is noticeable in a sharp change of the meteorological parameters. And in the latitudinal profile, the polynya effect on the parameters during north-directional air transport can be visually assessed. (Fig. 1). Ultimately, we can conclude that winter flow of cold air masses from the continent noticeably heat up over the polynya in the Laptev Sea and with further northward movement over drifting ice continues to warm. The warming effect extends only to the surface air layer from the surface level to 950 hPa. A consequence of the influx of heat from the polynya is the increase in heat transfer to the north in the region of 74° N with respect to the transfer through 70° N (Table 1). In the moisture transfer, it is found that the maximum values fall precisely over the area of the polynya, which is due to evaporation from the open water surface.

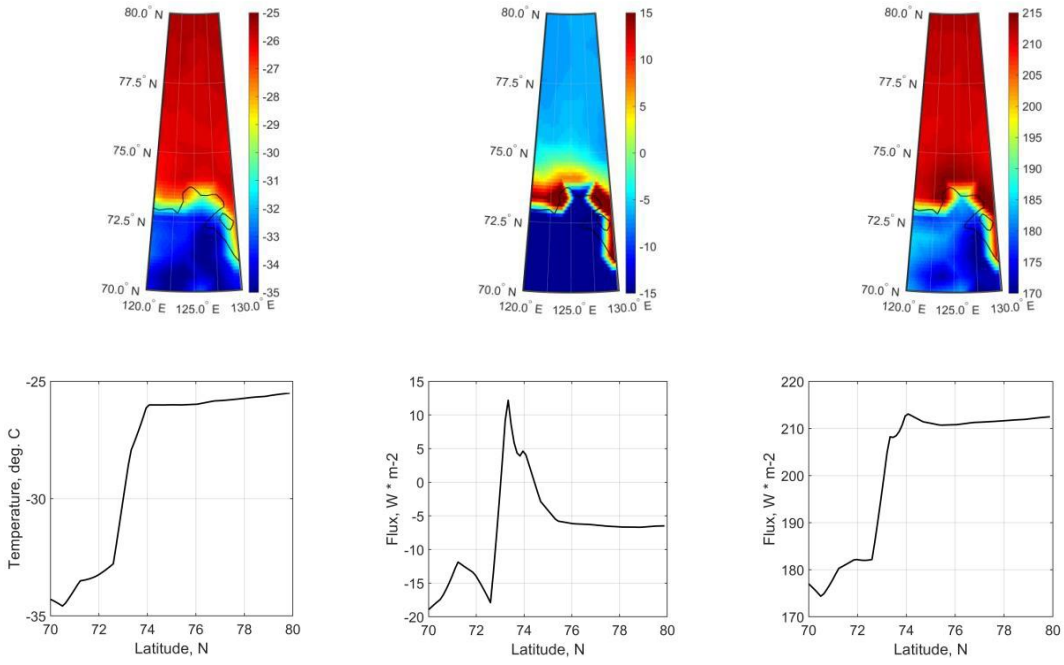

a. b. c.

Figure 1. Spatial distribution and latitudinal profile of surface temperature (a.), sensible heat flux (b.), outgoing longwave radiation (c.) from 1979 to 2018 in the Laptev sea region.

This confirms the assumption [1] that the winter transport of cold air from the mainland doesn't have strong cooling effect on the average winter air temperature north of 70 ° N due to the warming effect of the polynya.

References:

[1] Alekseev G.,Kuzmina S.,Bobylev L.,Urazgildeeva A., Gnatiuk N. Impact of atmospheric heat and moisture transport on the Arctic warming. Int. J Climatol., 2019, pp. 1—11, https://doi.org/10.1002/joc.6040

[2] Nakamura N., Oort A. H. Atmospheric heat budgets of the polar regions //Journal of Geophysical Research: Atmospheres. – 1988. – Т. 93. – №. D8. – С. 9510-9524.

[3] Marchuk G.I., Kondratiev K.Ya., Kozoderov V.V. Earth's radiation balance, key aspects. - M.: Nauka, 1988 .- 216 p.

[4] Makstas A.P. Thermal balance of arctic ice in winter. L.: Gidrometeoizdat, 1984. 66 p.

Combining precipitation fields on the basis of radar data and mesoscale model output products in nowcasting systems of Hydrometcenter of Russia

Alexander V. Smirnov, Anatoly V. Muravev, Dmitry B. Kiktev
Hydrometcenter of Russia
Email: smirnov@mecom.ru

Systems of two types for mesoscale deterministic and probabilistic nowcasting have been developed and operationally run at the Hydrometcenter of Russia over the past few years. The first type systems are built on the numerical weather prediction (NWP) output products adjusted to the latest ground observations. The second type systems are oriented on precipitation forecasting based on the DMRL-S radar data combined with the NWP output products. Description of these systems and their verification results, starting from the meteorological support of the Sochi Olympic Games in 2014, are overviewed in [Kiktev et al., 2017, Kiktev et al., 2019].

One of the well known and challenging problems for developing precipitation nowcasting systems lies in combing spatial areas pertaining to principally different sources and exhibiting diverse and hardly comparable spatiotemporal scales. In the context of the precipitation nowcasting system implemented at the Hydrometcenter of Russia this problem is aggravated by the fact that the Lagrangian extrapolation block of the "seamless" forecasting, i.e. the STEPS model [Bowler et al., 2006], starts with individual radars with a further formation of a unified field that covers the whole forecast area. It is here necessary: to take into account the circular radar surveys distribution over the forecast region, to transform those areas to quasi-rectangular fields (two dimensional arrays), to mark off or data fill the areas with missing values, keeping in mind evolutionary details over the forecast period, to recalculate intensity values in the overlapping zones, etc. The very-short-term forecasting interval (extending the two hour nowcasting period up to six hours) produces a similar problem of merging the unified radar field with the NWP output field.

Since the end of 2019 the precipitation nowcasting area with 9 DMRL-C radars covering the Central federal district (CFD), has been broadened to the European territory of Russia covered by 28 DMRL-S radars. By that time, a new STEPS version [Pulkkinen et al., 2019] had been adapted, which provided means to solve different extrapolation problems and to get around the difficulties in constructing composite fields.

In the first half of 2020 new testing of the Lagrangian block of the nowcasting system together with the calculation package for combining heterogeneous fields was initiated. Computational experiments in combining radar data with the NWP products over the CFD in 2-km resolution area have started, with precipitation estimates flowing from twelve DMRL-S, and forecast fields – from the COSMO model [Rivin et al, 2015]. The forecasts are generated at 10-min intervals as in the operational nowcasting system, and at 10-min refreshing intervals, as the radar sensing data flow in. Parallel testing of probabilistic nowcasting on the one-kilometer grid is performed.

Figure 1 demonstrates very clear differences between two combination methods: the previous scheme generates a fatal "shock" effect from radar field borders when by the 70^{th} minute the forecast flow runs into a "void" square left by the malfunctioning Vnukovo radar, whereas no such effect is observed in the new scheme. Other differences in location and intensity are accounted for by differing optical flow forecasting variants.

Figure 2 shows synchronized precipitation intensity fields (mm/h) (a) in the unified radar observation field, (b) in the NWP forecast field, and (c) in the combined radar and NWP field at the 90 min lead-time. The merging of fields and the forecast quality may be considered quite satisfactory if the synchronized unified radar field is considered the "observational truth".

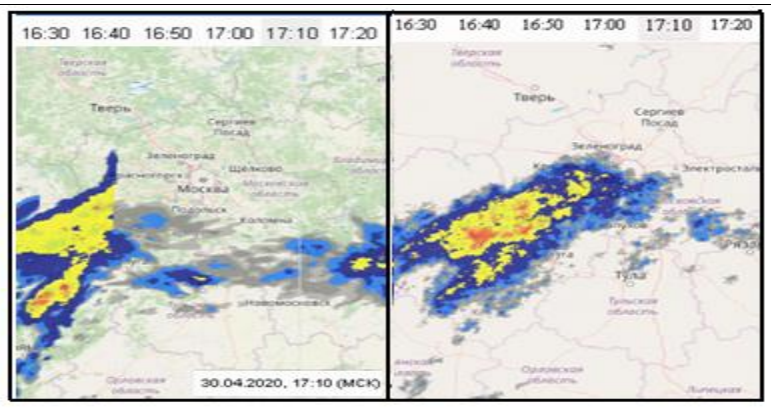

Figure 1. Forecast flow impingement against a "void" area left by the malfunctioning Vnukovo radar in the previous scheme (left), and in the new scheme (right), at 70 minutes lead-time.

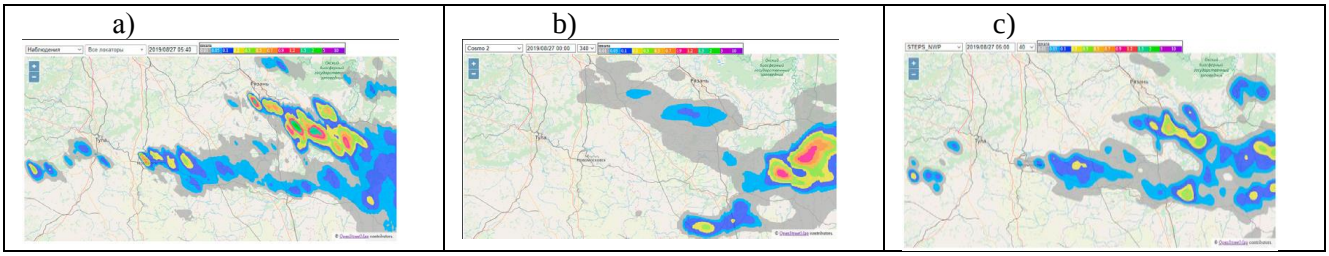

Figure 2. Examples of precipitation intensity forecast fields for synchronized time moments (panels left to right): radar observation field (a); numerical COSMO model forecast (b); blended forecast at 90 min lead-time (c).

References

1. *Bowler N., Pierce C., Seed A.* STEPS: A probabilistic precipitation forecasting scheme which merges an extrapolation nowcast with downscaled NWP // Q. J. R. Meteorol. Soc. 2006. Vol. 132. P. 2127-2155.

2. *Kiktev D., et all.* FROST-2014. The Sochi Winter Olympics International Project // BAMS. 2017. Vol. 98, no. 9. P. 1908-1929.

3. *Kiktev D. B., Murav'ev A. V., Smirnov A. V.* Nowcasting of meteorological parameters and hazards: implementation experience and development prospects // Gidrometeorologicheskie issledovaniya i prognozy [Hydrometeorological Research and Forecasting], 2019. № 4 (374). С. 92-111 [in Russ.].

4. *Pulkkinen S., D. Nerini, A.A. Pérez Hortal, C.Velasco-Forero, A. Seed, U. Germann, and L. Foresti*. Pysteps: an open-source Python library for probabilistic precipitation nowcasting (v1.0) // Geosci. Model Dev., 12, 4185–4219, 2019, https://doi.org/10.5194/gmd-12-4185-2019

5. *Rivin G.S.et al.* The COSMO-Ru system of nonhydrostatic mesoscale short-range weather forecasting of the Hydrometcenter of Russia: The second stage of implementation and development // Russ. Meteorol.Hydrol., 2015, vol. 40, no. 6, pp 400-410. DOI: 10.3103/S1068373915060060.

Impact of global warming on the Siberian rivers runoff

A. Vyazilova, G. Alekseev, N. Kharlanenkova, N. Glok
Arctic and Antarctic Research Institute, St. Petersburg, Russia
e-mail: vae@aari.ru

Introduction

Much attention is paid to the fresh water content (FWC) in the Arctic Ocean and its variations as FWC is a source of fresh water for the North Atlantic. The annual fresh water inflow to the Arctic Ocean is defined mainly by river runoff (42%), inflow through the Bering Strait (32%) and net precipitation (26%) (Serreze et al., 2006). Half of the annual river runoff into the Arctic accounts for the 3 large Siberian rivers: Ob, Yenisei, and Lena. The purpose of this research is to assess the impact of global and regional changes in atmospheric circulation, precipitation and air temperature on three major Siberian rivers runoff.

Data and methods

Data of surface air temperature and atmosphere moisture content from reanalysis ERA/Interim (Dee et al., 2011), global precipitation on land from PREC/L (Chen et al., 2002), and global precipitation climatology GPCC from the Global Precipitation Climatology Center (Adler et al., 2003) were used for investigation. Rivers discharge for the period 1936-2018 was received from the datasets R- ArcticNet (Lammers at al., 2016), ArcticGRO (Shiklomanov et al., 2018).

The catchment areas of 3 rivers and their total catchment area were approximated by the following geographical regions: Ob catchment area: 51.25-68.75° N, 61.25-88.75° E, Yenisei catchment area: 51.25-68.75° N, 91.25-108.75° E, Lena catchment area 51.25-68.75° N, 111.25-131.25° E, total catchment area: 50- 70° N, 60-160° E. The monthly mean surface air temperature and precipitation in the regions were defined. Indexes of zonal, meridional and general circulation in the northern hemisphere were calculated according to the monthly mean surface air temperature at the nodes of the geographical grid (Alekseev, 2014). Methods of multidimensional mutual-correlation and mutual-spectral analysis, calculation of low and high values repeatability of less than 10% and more than 90% probability were used.

Results

All correlation coefficients between the indexes and climatic parameters (mean values of air temperature, atmosphere moisture content and precipitation) at the catchment areas confirm the significant impact of atmospheric transports in the cold period of the year on surface air temperature, atmosphere moisture content and lesser on precipitation. In summer amplification of zonal circulation is accompanied by a decrease in the air temperature over the catchment areas while meridional transports enhance the air temperature even more than in winter. Whereas the winter zonal transport forms similar changes in mean air temperature, moisture content and precipitation in all regions of the catchment areas, in summer the changes have no connection in the Ob and Lena catchment areas.

The impact of surface air temperature and precipitation changes on the river runoff is estimated by correlation coefficients between mean air temperature, mean precipitation in the catchment areas and annual river discharge. Mostly mean annual precipitation affects the river runoffs, especially discharge of the river Lena (figure 1). Summer precipitation in June and July also affects.

The maximal positive trends of mean air temperature and precipitation in the catchment areas are observed in spring. Trend coefficient of mean air temperature in April is 0.11 °C in the Ob catchment area, 0.08 °C in the Lena catchment area, 0.10 °C in the Yenisei catchment area.

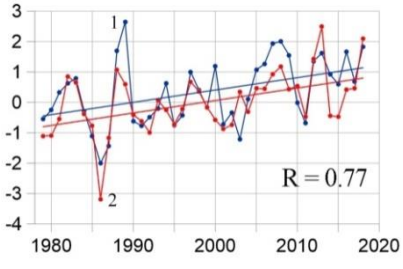

Figure 1. Correlation between annual Lena discharge and precipitation in the Lena catchment area (normalized data, 1 – discharge, 2 – precipitation)

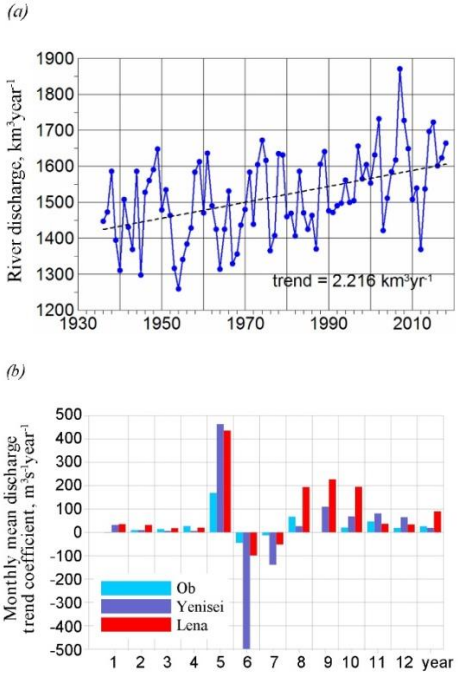

Figure 2. Total annual runoff of 3 rivers in 1936-2018 (*a*), monthly mean discharge trend coefficients, $m^3s^{-1}year^{-1}$ in 1979-2018 (*b*)

The positive trend indicates the increase of annual runoff of Ob, Lena and Yenisei. The trend is maximal for the Lena runoff (500.41 $m^3s^{-1}year^{-1}$ for 1936-2018 and 1079.73 $m^3s^{-1}year^{-1}$ for 1979-2018). Total annual runoff of 3 rivers was also increased during 1936-2018 (figure 2a) with the absolute maximum in 2007 and a linear trend of 2.216 km^3year^{-1}. Monthly runoff of 3 rivers increased in May. In June, when the runoff is maximum, the runoff of 3 rivers decreased in 1936-2018 and 1979-2018 (figure 2b). June trends in 1979-2018 are -51.77 $m^3s^{-1}year^{-1}$ for Ob, -98.86 $m^3s^{-1}year^{-1}$ for Lena, -387.36 $m^3s^{-1}year^{-1}$ for Yenisei.

To assess the frequency of the runoff maximums, the integral frequencies of low and high maximums of less than 10% and more than 90% probability function, respectively, were calculated. An increase in the number of low runoff maximums in 1940-50s and in the 2000s was found as well as an increase in the number of high maximums in 1970-1980s. It means that during warming low maximums dominate, while during cooling of climate the number of high maximums rises.

Conclusions

The effect of the atmospheric transport of heat and moisture is most prominent in the cold part of the year, especially in November and March. In summer, the increase of zonal transport is accompanied by a decrease of air temperature in the area of catchments, and meridional transport enhances the temperature. The atmospheric transport in winter leads to similar changes in the mean values of temperature, moisture content and precipitation in all catchment areas.

The greatest influence on runoff, especially on the Lena's runoff, is exerted by the increase of average annual precipitation. The effect of temperature changes is noticeable when annual temperature is averaged over all three basins. The annual discharge of rivers increases, especially the discharge of Lena. The total annual runoff of the three rivers was increasing during 1936–2018 with a rate of 2.216 km^3year^{-1}.

In the 2000s, the frequency of low maximums of runoff increased, while the frequency of high maximums decreased. The high occurrence of large maximums was noted in 1970–1980s. Such distribution of the frequency of low and high maximums is associated with climate warming in the 2000s and cooling in the 1970–1980s.

This study was supported by the Russian Foundation for Basic Research, project 18-05-60107.

References

Adler RF, Huffman GJ, Chang A, Ferraro R, Xie P-P, Janowiak JE, et al. 2003 The Version-2 Global Precipitation Climatology Project (GPCP) Monthly Precipitation Analysis (1979–Present). *J. Hydrometeorol.* 4(6):1147–67

Alekseev G.V. The Arctic Dimension of Global Warming. 2014 *Ice and Snow*. No. 2. C. 53—68 (in Russian)

Chen M, Xie P, Janowiak JE and Arkin P 2002 Global Land Precipitation: A 50-yr Monthly Analysis Based on Gauge Observations. *J. Hydrometeorol.* 3(3):249–66

Dee DP, Uppala SM, Simmons AJ, Berrisford P, Poli P, Kobayashi S, et al. 2011 The ERA-Interim reanalysis: Configuration and performance of the data assimilation system. *Q J R Meteorol. Soc.* 137:553–97

Lammers RB, Shiklomanov AI, Vörösmarty CJ, Fekete BM and Peterson BJ 2016 R-ArcticNet, A Regional Hydrographic Data Network for the Pan-Arctic Region (ISO-image of CD-ROM). PANGAEA. Available from: https://doi.org/10.1594/PANGAEA.859422

Serreze MC, Barrett AP, Slater AG, Woodgate RA, Aagaard K, Lammers RB, et al. 2006 The large-scale freshwater cycle of the Arctic. *J. Geophys. Res. Ocean* 111(C11010):1–19.

Shiklomanov AI, Holmes RM, McClelland JW, Tank SE and Spencer RGM 2018 Arctic Great Rivers Observatory. Discharge Dataset, Version 20190402. Available from: https://www.arcticrivers.org/data